Synthesis of metallic glass nanoparticles by inert gas condensation

Kaifeng Zheng and Paulo S. Branicio*

Mork Family Department of Chemical Engineering and Materials Science, University of Southern California, 3651 Watt Way, VHE 602 Los Angeles, California 90089-0242, USA

(Received 26 April 2020; accepted 9 June 2020; published 7 July 2020)

Inert gas condensation (IGC) is a versatile method for the synthesis of ultrafine nanoparticles. While it has been mostly used in the synthesis of nanocrystalline particles, it has also been employed in the synthesis of metallic glass nanoparticles, which can be further used in the generation of nanostructured metallic glasses, known as nanoglasses. In this work, we use molecular dynamics simulations to investigate the IGC processes leading to the synthesis of $Cu_{64}Zr_{36}$ amorphous nanoparticles. We investigate the growth of nanoparticles up to 7.3 nm diameter using long simulations of up to 130 ns, under relatively low pressures in the range of 4–10 bars. Results indicate a significant effect of pressure on the final structure of the amorphous nanoparticles, yet no clear influence on the segregation of Cu atoms to its surface. Cu segregation occurring at all pressures results in a thin Cu-rich layer, about 2.5 Å thick, that coats all nanoparticles. Statistics of atomic Voronoi polyhedra shows that the fraction of full icosahedra in the nanoparticles produced at 4 bars is equivalent to that of bulk metallic glasses produced by melt and quench at 10^9 K/s. Higher pressures result in a lower fraction of full icosahedra.

DOI: 10.1103/PhysRevMaterials.4.076001

I. INTRODUCTION

Functional metal nanoparticles have been widely investigated for applications in biomedicine [1], catalysis [2], and other fields [3,4]. Nanoparticles can be synthesized by employing chemical methods [5,6] or physical methods such as inert gas condensation (IGC) [7]. IGC has been used extensively in recent years, in particular in the synthesis of nanostructured particles [8,9]. In the IGC method, a metal is used as a vapor source, which is commonly produced by thermal evaporation, and a chamber with a low-pressure cold inert gas is used to condense the vapor and form nanoparticles [10]. The supersaturated vapor can also be generated by other means such as magnetron sputtering [9] and laser ablation [11,12]. Pioneering work on nanocrystalline materials used IGC to synthesize a wide range of ultrafine metallic, ceramic, and composite materials [13–15].

Due to the challenges in the characterization and monitoring of the synthesis of nanoparticles from vapor phase using *in situ* experiments, modeling and simulation of these processes are becoming increasingly essential [16]. Krasnochtchekov *et al.* applied molecular dynamics (MD) to the study of the generation of Ge, Cu, and Cu-Ag alloy nanoparticles in an Ar atmosphere [10]. Their results showed explicitly Ag surface segregation in crystalline Cu-Ag nanoparticles. Further modeling investigations described the production of nanoparticles containing Cu [17,18], Ag [19], Si [20], and other elements [21,22]. The kinetics involved in the nucleation and growth processes of metallic systems in an inert gas environment have been the focus of many modeling investigations [10,18,22]. Recently, Mattei *et al.* [23] reported a systematic investigation of the Au, Pt, and Pb ternary system. They reported MD and Monte Carlo simulation results on the generation of nanoparticles with different structures at various compositions of Au, Pt, and Pb atoms by magnetron sputtering inert gas condensation. Although there are many simulation reports on the IGC generation of crystalline nanoparticles, it is still not understood how amorphous nanoparticles are generated. Those particles became particularly relevant after the advent of metallic nanoglasses [24–28] and the demonstration of their unusual mechanical properties [29–34].

In this work, we used MD simulations to tackle the problem of describing the IGC formation of $Cu_{64}Zr_{36}$ amorphous nanoparticles. Such nanoparticles are the basic ingredient of nanoglasses, which are generated by cold consolidation of amorphous nanoparticles [28]. The simulation results describe in detail the formation and the final structure of $Cu_{64}Zr_{36}$ amorphous nanoparticles produced under pressures from 4 to 10 bars. Focus is given to the analysis of local atomic packing and surface segregation. In addition, we discuss the topology of amorphous nanoparticles in terms of their statistics of atomic Voronoi polyhedra and how they compare to that of metallic glass structures produced by conventional melting-quenching procedures.

II. COMPUTATIONAL METHOD

All MD simulations are performed with LAMMPS [35]. Data analyses are performed with post run PYTHON scripts and within OVITO [36], which is also used for visualizations. Simulations are carried out with inert gas particles at 300 K at three different initial pressures: 4, 6, and 10 bars. To set up the initial system, 11 400 Cu and Zr atoms are distributed at random positions in the simulation box at a Cu:Zr ratio

*branicio@usc.edu

of 64:36. Such a number of metal atoms is sufficient to generate a final 7-nm-sized nanoparticle. Argon is selected as the inert gas, following previous MD simulations of inert gas condensation [17,18,20,22,23]. Initially, 11 400 Ar atoms are also distributed randomly in the simulation box.

We follow the procedures discussed by Kesälä *et al.* [17] to determine the simulation box size and initial pressure using the Virial theorem. We use as initial pressure 4, 6, and 10 bars and corresponding simulation cubic boxes with 49.1, 43.1, and 36.2 nm side lengths. Periodic boundary conditions (PBCs) are applied in all x, y, and z directions. It is worth mentioning that the pressure utilized in experiments of inert gas condensation of nanocrystalline particles is extremely low, typically in the range 1–100 mbar [17]. In our work, the selected pressures, in the few bars range, yield much larger cooling rates, which are required to avoid crystallization and produce amorphous structures.

To model the IGC process, we follow a procedure similar to that detailed in the work of Kesälä *et al.* [17] and Mattei *et al.* [23]. We use a Berendsen thermostat to keep the temperature of Ar atoms constant at 300 K, turning them into a heat sink. While more elaborate and accurate algorithms such as the Nosé-Hoover have been used in IGC simulations [23], the Berendsen thermostat offers a simple and robust algorithm that efficiently keep temperature under control in nonequilibrium processes such as IGC. The Berendsen thermostat has been used successfully in earlier IGC simulations [17,20]. The temperature of the metal atoms is controlled indirectly by the collisions with the inert gas atoms and exchange of kinetic energy. To accelerate the formation of a nanoparticle, we enhance the rate of collisions between metal atoms by applying a small dragging force of 10^{-6} eV/Å to all metal atoms. The magnitude of the force is less than 1% of the typical interatomic force magnitude. The force pulls metal atoms into a spherical region in the center of the simulation box with a 3.5 nm radius, the predicted radius of a formed particle. The atoms in the spherical region are free from any external force. This external force enhances the rate of collision of metal atoms in the middle of the box and shortens the total simulation time to achieve a single particle in the system while not affecting its structure. The choice of a time step in MD simulations is critical since it influences directly the accuracy of the simulation results. In this work, the choice of a suitable time step is challenging given the combination of collisions between high-velocity particles and the presence of atoms and clusters with large temperature differences. We used a dynamic time step with an initial and maximum value of 1 fs, which is reduced as needed to keep the atomic displacements to less than 0.1 Å per time step, and thus maintain the stability of the integration of the equations of motion. The embedded atom model potential developed by Cheng and Ma [37] is employed to describe the interactions between metal atoms. This potential has been widely validated in investigations of CuZr systems [32,38,39]. Meanwhile, the interactions between metal and Ar atoms are purely repulsive following the ZBL potential [40]. The forces between Ar atoms are described by Lennard-Jones interaction with $e = 0.0123$ eV, $a = 3.76$ Å, and a cutoff distance of 10 Å [18].

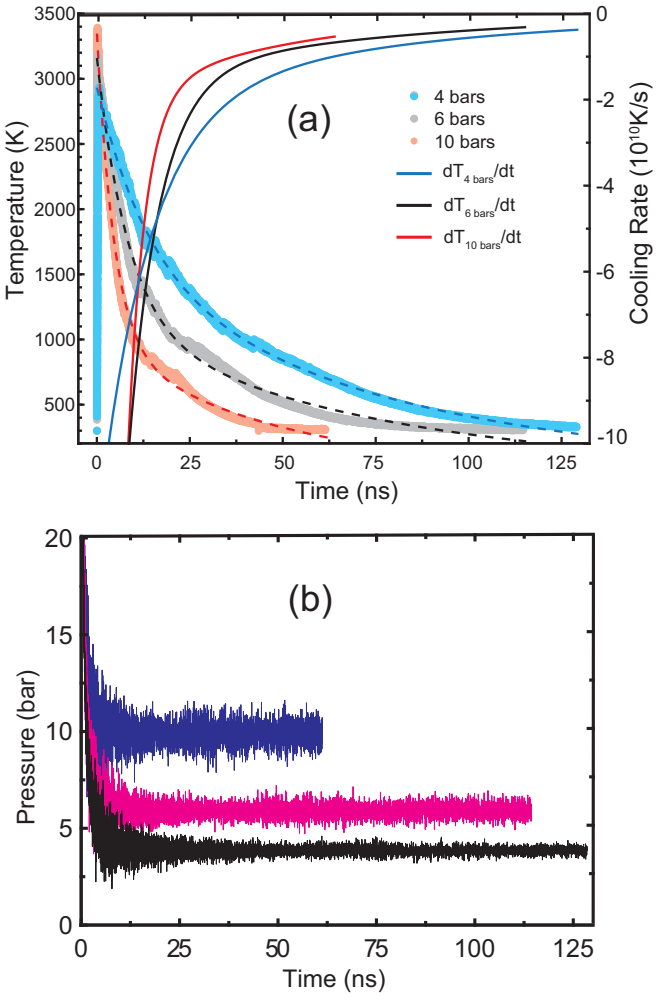

FIG. 1. The evolution of temperature and pressure during the inert gas condensation (IGC) process. (a) Temperature profiles for metallic species as a function of time for IGC pressure of 4, 6, and 10 bars. The cyan, gray, and orange circle lines indicate the temperature evolution in the IGC simulations (left y-axis). Dashed lines are fitted curves to the temperature profiles data. Solid lines are derivatives of the fitted temperature curves and indicate the dynamic cooling rates of the IGC processes (right y-axis). (b) Pressure profiles as a function of time for the IGC processes, at 10 bars (blue line), 6 bars (magenta line), and 4 bars (black line).

III. RESULTS AND DISCUSSIONS

A. Inert gas condensation process

In the initial configuration of the IGC process, Ar, Cu, and Zr atoms are distributed randomly in the simulation box, and the atomic kinetic energy is set following a Maxwell-Boltzmann velocity distribution to produce a system temperature of 300 K. The system state changes rapidly as metal atoms immediately form bonds and clusters after the initial atomic collisions, releasing heat and raising sharply the temperature in the first nanoseconds of simulation. As shown in Fig. 1(a), the temperature of the metallic species reaches over 3000 K for all pressures considered. As the temperature of the Ar gas is kept fixed at 300 K, the heat released by the formation of metallic bonds and clusters is gradually dissipated, lowering the temperature at a rate that depends

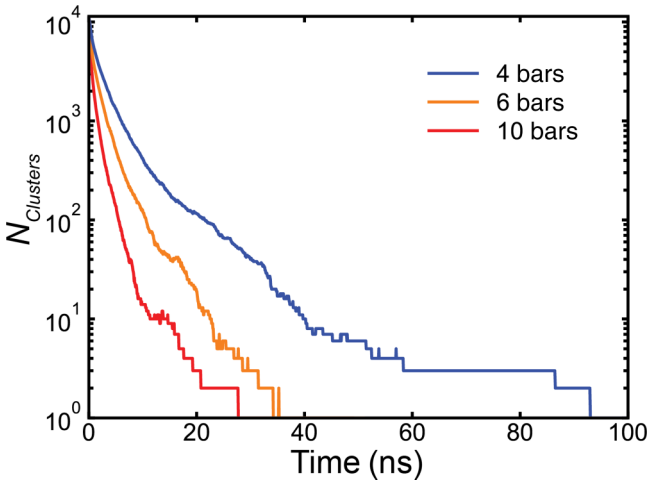

FIG. 2. Kinetics of clustering in the IGC processes at different pressures. The plot illustrates the number of clusters as a function of condensation time.

directly on the gas pressure [41]. The measured decline in temperature of metallic species at 4, 6, and 10 bars is shown by cyan, gray, and orange thick lines in Fig. 1(a). Dashed lines overlapping each one of the curves are fitted functions to the data. As one can see, at a pressure of 4 bars it takes about 130 ns of simulation time to cool down the metallic species to 300 K. The total simulation time to complete the same cooling is reduced to about 115 and 62 ns for 6 and 10 bars, respectively. The dynamic cooling rate for each pressure value, calculated by applying a time derivative to the fitted curves of temperature versus time, is shown by the solid lines in Fig. 1(a). The cooling rate in all cases is in the order of $\sim 10^{10}$ K/s for most of the condensation process and the nanoparticle generation. Both the maximum temperature and the cooling rate of the metallic system are dictated by the condensation gas pressure, as it defines the atomic mean free path and the rate of collisions, indicated by the following equation:

$$\lambda = \frac{RT}{\sqrt{2}\pi d^2 N_A P},$$

where R is the universal gas constant, T is the temperature, d is the effective diameter of the gas atoms, N_A is Avogadro's number, and P is the gas pressure [42]. At the very beginning of the simulation, when the temperature increases sharply, the system pressure also increases sharply, as shown in Fig. 1(b). As the Ar gas temperature is controlled and kept constant at 300 K, the pressure stabilizes after a few nanoseconds of simulation time and fluctuates around the target values.

As the metallic species collide, make new bonds, and release heat intensely in the first nanoseconds of simulation, they form clusters of increasing size. Details on the metallic cluster nucleation and grow kinetics and their final morphology are provided in Figs. 2 and 3. As expected, the inert

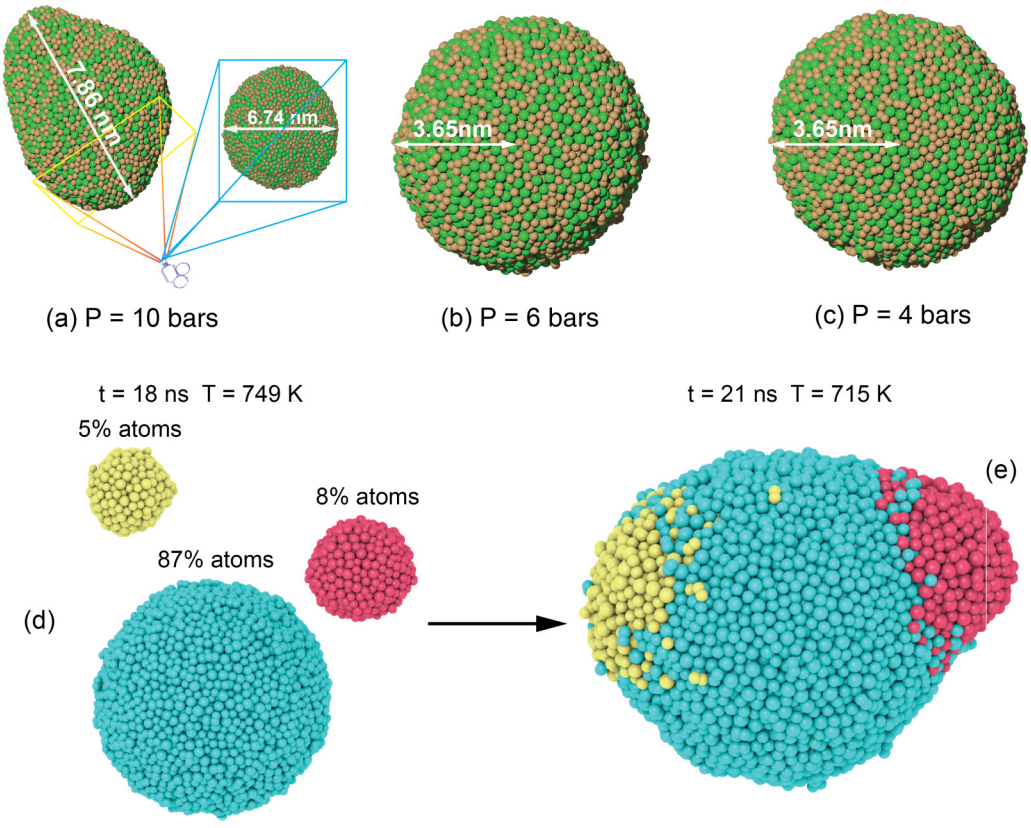

FIG. 3. Illustrations of the nanoparticles generated during the IGC processes at 10, 6, and 4 bars. (a)–(c) Illustrations of final particles generated by IGC at 10, 6, and 4 bars, respectively. Different colors denote different atomic species, i.e., Zr is colored green and Cu is brown. (d),(e) Final aggregation process at 10 bars leading to an irregular shaped particle from 18 to 21 ns condensation time. Different colors denote different clusters.

gas pressure has a strong influence on the clustering rate, as shown in Fig. 2(a). The condensation process at 10 bars is completed in just 30 ns, resulting in a single cluster. In contrast, the condensation process requires nearly 100 ns to be completed under 4 bars. During the aggregation and clustering process the initial temperature spike is dissipated, and while the temperature is reduced large clusters absorb metallic atoms and smaller clusters continually until a dominant single cluster is generated. At that point in time, the simulations show that the single nanoparticles still require a long time to cool down to 300 K, implying that their structure still evolves and relaxes until room temperature is achieved. However, in the range of pressures considered in this work we can identify important distinct processes. While the nanoparticles generated under 4 and 6 bars have a regular, nearly spherical shape, the nanoparticles generated under 10 bars display a rather irregular shape. Analyses indicate that the cause of the contrast in final nanoparticle shapes is the rapid cooling experienced by the clusters during the aggregation process. At 18 ns, when the temperature of the metallic species is reduced to the glass-transition temperature, $T_g = 800$ K [32], the largest cluster has about 87% of all metal atoms. The remaining atoms are located in two smaller clusters, as shown in Fig. 3(d). As the aggregation process progresses, at 21 ns a single nanoparticle is formed below T_g; see Fig. 3(d). The limited diffusivity below T_g constrains the structural relaxation, and the final shape of the nanoparticle at 300 K is asymmetrical and irregular. In contrast, the nanoparticles in the 4- and 6-bars cases, formed above T_g, form nearly perfect spherical shapes and have identical 3.65 nm radii, as shown in Figs. 3(b) and 3(c).

B. Analysis of the generated nanoparticles

1. Structural correlations

We performed different analyses on the generated nanoparticles to assess their structure, composition, and the effects of condensation pressure. At first, it is important to verify the presence and extent of short-, medium-, and long-range order in the structure to verify the formation of the expected amorphous structure consistent with a metallic glass. For that purpose, we analyzed structural correlations in the generated nanoparticles by calculating the radial distribution function, $g(r)$, which provides valuable information about the short-, medium-, and long-range order in the structure of the material. The partial $g(r)$, accounting separately for structural correlations between Cu-Zr, Cu-Cu, and Zr-Zr pairs of atoms, is shown in Fig. 4. As one can see, the presence of a well-defined first peak in the plots indicates clearly the presence of short-range order in the structure of all nanoparticles. The presence of medium-range order is implied as well by the occurrence of a second and third peak with additional features in between them in all partial $g(r)$ curves. Combined with the lack of long-range order, the set of $g(r)$ displayed in Fig. 4 suggests that the structure of the nanoparticles follows the typical signatures of the amorphous structure of a metallic glass [37]. As shown in Fig. 4, the pressure of the inert gas has a negligible effect on the $g(r)$, and consequently on the structural correlations. The result is comparable to reported x-ray diffraction of $Cu_{63.5}Zr_{35.5}$ [43]. The results from the

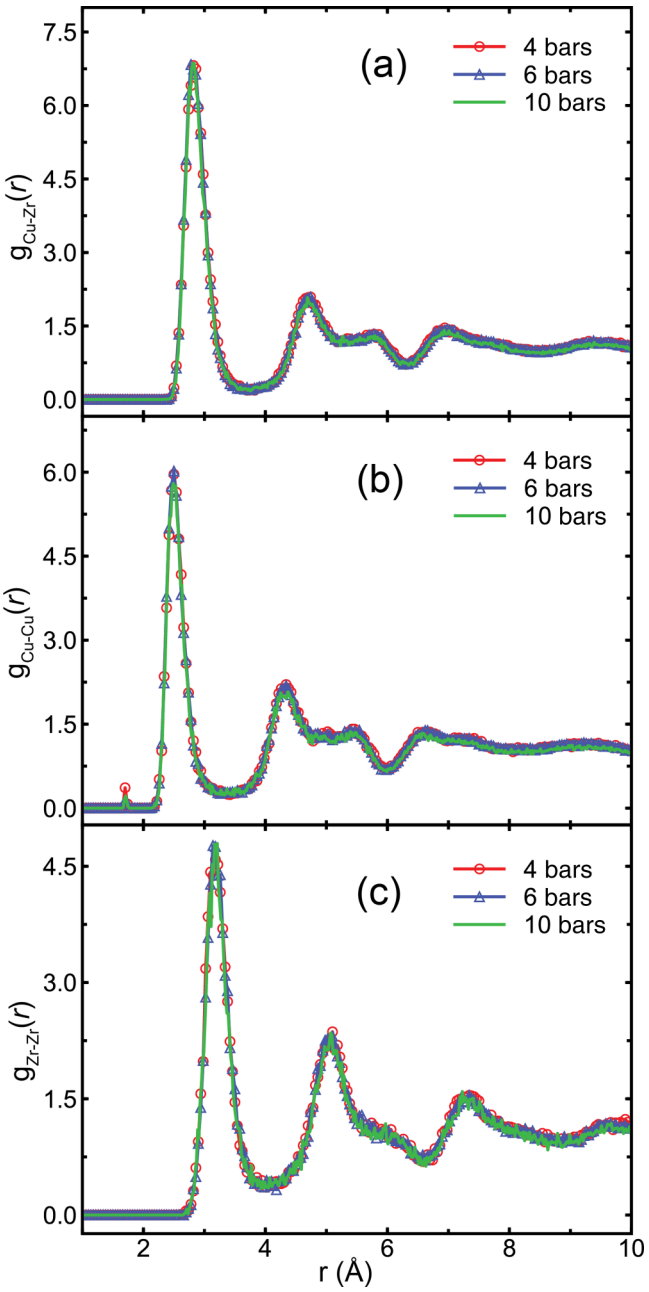

FIG. 4. Partial pair distribution function of the nanoparticles formed at different pressures. (a) Partial distribution function for Cu-Zr pairs, (b) Cu-Cu pairs, and (c) Zr-Zr pairs.

partial $g_{Cu-Cu}(r)$ indicate a minor peak at ~1.8 Å. Further analysis of the few pairs of atoms with this bond length in the nanoparticle indicates that they are all present on the surface shell where Cu segregation forms a thin layer. As Cu-Cu bond lengths are >2 Å, it seems that the presence of these Cu-Cu surface bonds at 1.8 Å is an artifact of the potential used for the specific conditions encountered at the surface.

2. Voronoi tessellation

Further information about the amorphous structure can be obtained from the statistics of atomic Voronoi polyhedra formed considering the bond topology [32,37,43,44].

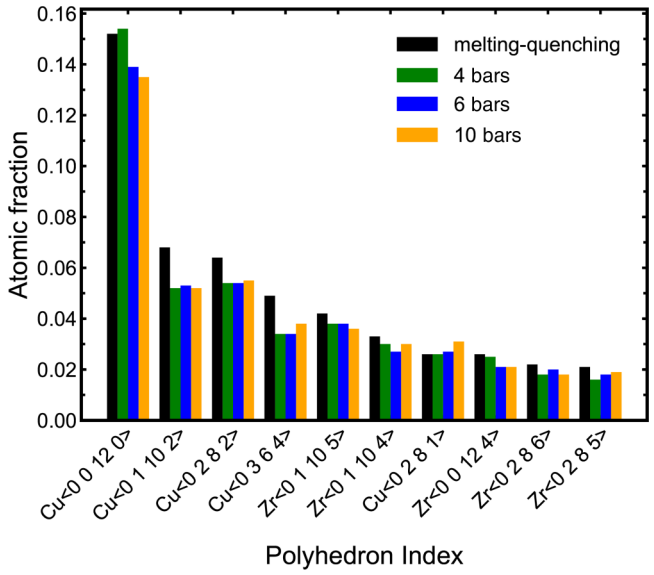

FIG. 5. Statistics of the atomic Voronoi polyhedra showing the 10 most prevalent polyhedra for the structure of the three nanoparticles formed at 10, 6 and 4 bars. Data for the $Cu_{64}Zr_{36}$ metallic glass generated by melting-quenching are also shown as a reference.

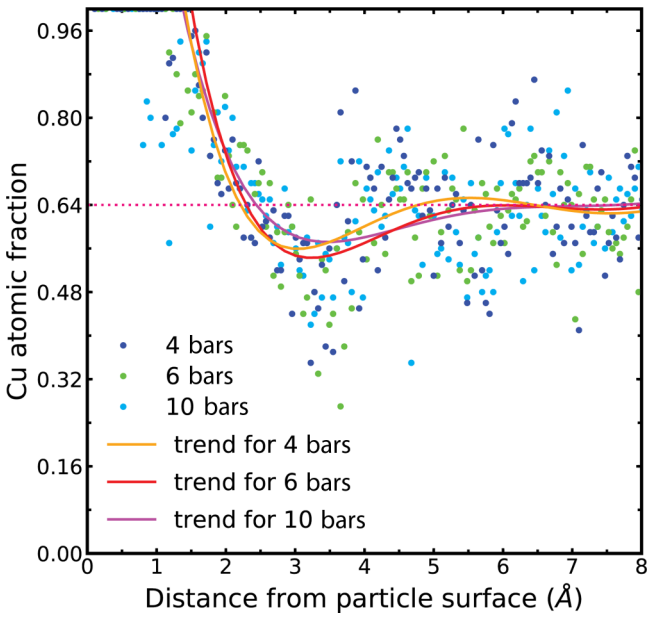

FIG. 6. Cu surface segregation for the final nanoparticles generated in the IGC. Solid curves indicate the trends of Cu atomic fraction from the surface to the bulk of the nanoparticles generated at 4, 6, and 10 bars.

For instance, for Cu-rich CuZr metallic glasses, the Cu full icosahedra (FI), denoted Cu⟨0,0,12,0⟩, is the most prevalent polyhedron and has been associated with the strength and brittleness displayed by the metallic glass [45]. We calculate the statistics of the most prevalent polyhedra found in the structure of the nanoparticles. The results are shown in Fig. 5 and display the corresponding atomic fraction of the ten most prevalent polyhedra. As a reference, we also show in Fig. 5 the statistics of the same polyhedra calculated from a metallic glass sample prepared using a melting-quenching procedure under a constant cooling rate of 10^9 K/s [32]. The results indicate that the concentration of FI in the IGC nanoparticles increases inversely with the pressure. The total fraction of FI in the nanoparticle generated under 4 bars is equivalent to that in the reference metallic glass sample. The remaining prevalent atomic Voronoi polyhedra have equivalent fractions for all the nanoparticles, indicating that the structure is structurally equivalent for most purposes. The fractions are also consistently smaller than that of the melting-quenching sample, suggesting that the medium-range order is better established in the melting-quenching procedure than using the IGC process. Nonetheless, in most cases the difference is almost negligible, indicating that the amorphous structures produced following both procedures are equivalent for most purposes.

3. Cu surface segregation

In addition to characterizing the structure of the amorphous nanoparticles, it is important to investigate possible variations in the chemical composition throughout the nanoparticle. In particular, surface segregation of species in multicomponent nanoparticles generated by IGC is a common phenomenon [44]. Several investigations of crystalline nanoparticles have reported surface segregation and the generation of a well-defined species rich surface layer [10,23,44,46]. Amorphous nanoparticles generated by IGC are believed to develop surface segregation as well. Nonetheless, a direct demonstration of surface segregation in amorphous alloy nanoparticles as well as a detailed description of composition variation from the surface of the nanoparticle is still missing. According to Adjaoud and Albe [44], Cu is segregated to the surface of CuZr nanoparticles, and the driving force for the segregation process is the cohesive energy. Arguably, Cu segregates to the surface because of its lower associated cohesive energy [43,44]. This argument has thermodynamic support since the lower cohesive energy is related to a lower melting point. In fact, while pure copper melts at ∼1358 K, pure zirconium melts at a much higher temperature of ∼ 2128 K. That implies that during the fast cooling, used to produce the amorphous nanoparticles, copper atoms will have higher mobility than Zr, which will tend to be concentrated in the core of the nanoparticles. That mechanism also explains the formation of nonequilibrium alloy microstructures with cored grains during quenching [47,48].

We investigated the chemical composition variation in all three generated nanoparticles generated under different pressures, and the results show in all cases the formation of a thin Cu segregation layer on the surfaces. To quantify the Cu segregation layer chemical variation and thickness, we evaluate the Cu concentration from the surface to the core of the nanoparticles [41]. The irregular shape of the particle generated under 10 bars poses a challenge to the calculation of the concentration from the surface. To overcome that, we employed a correlation model by using the spherical nanoparticles as a reference.

The result displayed in Fig. 6 indicates that significant average deviations in Cu segregation only occur in a very thin

region ∼0.5 nm thick close to the surface. At the surface of the nanoparticles, surface segregation is clearly identified as the Cu atomic fraction rises to much higher levels than the 0.64 average composition of the alloy. The result is a well-defined nearly monatomic thick layer at the surface. The data in Fig. 6 suggest that the shape of the nanoparticle and the IGC gas pressure have negligible effects on the segregation process.

IV. CONCLUSION

In this work, we used molecular dynamics simulations to characterize the synthesis of $Cu_{64}Zr_{36}$ amorphous nanoparticles by inert gas condensation. The results from simulations at 4-, 6-, and 10-bars pressure indicate that the cooling rates and clustering rates increase with system pressure. A relative high pressure of 10 bars resulted in an irregularly shaped nanoparticle, while simulations at 4 and 6 bars resulted in rather spherical-like particles. Cu surface segregation was observed in all cases, resulting in a monatomic coating layer at the nanoparticle surface. Atomic Voronoi polyhedra analysis indicated that the concentration of full icosahedra increases as the pressure and associated cooling rates decrease. The fraction of full icosahedra in the nanoparticle produced at 4 bars is equivalent to that in bulk metallic glass produced by melting-quenching with a cooling rate of 10^9 K/s. These results shine light on the kinetics and the mechanisms of amorphous nanoparticle formation and growth in inert gas condensation.

ACKNOWLEDGMENTS

This material is based upon work supported by the U.S. Department of Energy, Office of Science, Office of Basic Energy Sciences, under Award No. DE-SC0020295. Computation for the work described in this paper was supported by the University of Southern California's Center for High-Performance. The authors gratefully acknowledge helpful discussions with Horst Hahn.

[1] P. V. AshaRani, G. Low Kah Mun, M. P. Hande, and S. Valiyaveettil, ACS Nano **3**, 279 (2009).
[2] J. Yin, S. Shan, L. Yang, D. Mott, O. Malis, V. Petkov, F. Cai, M. Shan Ng, J. Luo, B. H. Chen, M. Engelhard, and C.-J. Zhong, Chem. Mater. **24**, 4662 (2012).
[3] C. Clavero, Nat. Photon. **8**, 95 (2014).
[4] F. Brandl, N. Bertrand, E. M. Lima, and R. Langer, Nat. Commun. **6**, 7765 (2015).
[5] H. Ohde, F. Hunt, and C. M. Wai, Chem. Mater. **13**, 4130 (2001).
[6] S. Mourdikoudis and L. M. Liz-Marzán, Chem. Mater. **25**, 1465 (2013).
[7] E. Pérez-Tijerina, M. Gracia Pinilla, S. Mejía-Rosales, U. Ortiz-Méndez, A. Torres, and M. José-Yacamán, Faraday Discuss. **138**, 353 (2008).
[8] B. Skårman, T. Nakayama, D. Grandjean, R. E. Benfield, E. Olsson, K. Niihara, and L. R. Wallenberg, Chem. Mater. **14**, 3686 (2002).
[9] J. Zhao, E. Baibuz, J. Vernieres, P. Grammatikopoulos, V. Jansson, M. Nagel, S. Steinhauer, M. Sowwan, A. Kuronen, K. Nordlund, and F. Djurabekova, ACS Nano **10**, 4684 (2016).
[10] P. Krasnochtchekov, K. Albe, and R. S. Averback, Z. Met. **94**, 1098 (2003).
[11] Z. Pászti, G. Petõ, Z. E. Horváth, and A. Karacs, Appl. Surf. Sci. **168**, 114 (2000).
[12] A. Ceylan, A. K. Rumaiz, and S. Ismat Shah, J. Appl. Phys. **101**, 094302 (2007).
[13] R. Birringer, H. Gleiter, H.-P. Klein, and P. Marquardt, Phys. Lett. A **102**, 365 (1984).
[14] J. Karch, R. Birringer, and H. Gleiter, Nature (London) **330**, 556 (1987).
[15] U. Herr, J. Jing, R. Birringer, U. Gonser, and H. Gleiter, Appl. Phys. Lett. **50**, 472 (1987).
[16] M. T. Swihart, Curr. Opin. Colloid Interface Sci. **8**, 127 (2003).
[17] E. Kesälä, A. Kuronen, and K. Nordlund, Phys. Rev. B **75**, 174121 (2007).
[18] A. E. Korenchenko, A. G. Vorontsov, B. R. Gelchinski, and G. P. Sannikov, Physica A **496**, 147 (2018).
[19] M. Á. Gracia-Pinilla, E. Pérez-Tijerina, J. Antúnez-García, C. Fernández-Navarro, A. Tlahuice-Flores, S. Mejía-Rosales, J. M. Montejano-Carrizales, and M. José-Yacamán, J. Phys. Chem. C **112**, 13492 (2008).
[20] J. Zhao, V. Singh, P. Grammatikopoulos, C. Cassidy, K. Aranishi, M. Sowwan, K. Nordlund, and F. Djurabekova, Phys. Rev. B **91**, 035419 (2015).
[21] M. Abbaspour, H. Akbarzadeh, S. Salemi, and S. Lotfi, Ind. Eng. Chem. Res. **57**, 14837 (2018).
[22] G. Rollmann, R. Meyer, and P. Entel, Phase Trans. **78**, 733 (2005).
[23] J.-G. Mattei, P. Grammatikopoulos, J. Zhao, V. Singh, J. Vernieres, S. Steinhauer, A. Porkovich, E. Danielson, K. Nordlund, F. Djurabekova, and M. Sowwan, Chem. Mater. **31**, 2151 (2019).
[24] J. Jing, A. Krämer, R. Birringer, H. Gleiter, and U. Gonser, J. Non. Cryst. Solids **113**, 167 (1989).
[25] G. Y. Wu, J. Z. Jiang, and X. P. Lin, Nanostruct. Mater. **12**, 843 (1999).

[26] J. X. Fang, U. Vainio, W. Puff, R. Würschum, X. L. Wang, D. Wang, M. Ghafari, F. Jiang, J. Sun, H. Hahn, and H. Gleiter, Nano Lett. **12**, 458 (2012).
[27] N. Chen, D. V. Louzguine-Luzgin, G. Q. Xie, P. Sharma, J. H. Perepezko, M. Esashi, A. R. Yavari, and A. Inoue, Nanotechnology **24**, 045610 (2013).
[28] O. Franke, D. Leisen, H. Gleiter, and H. Hahn, J. Mater. Res. **29**, 1210 (2014).
[29] O. Adjaoud and K. Albe, Acta Mater. **168**, 393 (2019).
[30] O. Adjaoud and K. Albe, Acta Mater. **145**, 322 (2018).
[31] S. Adibi, Z. D. Sha, P. S. Branicio, S. P. Joshi, Z. S. Liu, and Y. W. Zhang, Appl. Phys. Lett. **103**, 211905 (2013).
[32] S. Adibi, P. S. Branicio, Y.-W. W. Zhang, and S. P. Joshi, J. Appl. Phys. **116**, 043522 (2014).
[33] S. Adibi, P. S. Branicio, and S. P. Joshi, Sci. Rep. **5**, 15611 (2015).
[34] Z. D. Sha, P. S. Branicio, Q. X. Pei, Z. S. Liu, H. P. Lee, T. E. Tay, and T. J. Wang, Nanoscale **7**, 17404 (2015).
[35] S. Plimpton, J. Comput. Phys. **117**, 1 (1995).
[36] A. Stukowski, Model. Simul. Mater. Sci. Eng. **18**, 015012 (2010).
[37] Y. Q. Cheng and E. Ma, Prog. Mater. Sci. **56**, 379 (2011).
[38] Y. Q. Cheng, E. Ma, and H. W. Sheng, Phys. Rev. Lett. **102**, 245501 (2009).
[39] Y. Fan, T. Iwashita, and T. Egami, Phys. Rev. E **89**, 062313 (2014).
[40] J. F. Ziegler and J. P. Biersack, *Treatise Heavy-Ion Science* (Springer, Boston, 1985), pp. 93–129.
[41] See Supplemental Material at http://link.aps.org/supplemental/10.1103/PhysRevMaterials.4.076001 for details on temperature change at the onset of the inert gas condensation and on the method used to quantify Cu surface segregation.
[42] W. A. Alexander, *Physics and Chemistry of Gas-Liquid Interfaces* (Elsevier, Amsterdam, 2018), pp. 195–243.
[43] J. Ding, Y.-Q. Cheng, and E. Ma, Acta Mater. **69**, 343 (2014).
[44] O. Adjaoud and K. Albe, Acta Mater. **113**, 284 (2016).
[45] M. Jafary-Zadeh, R. Tavakoli, D. J. Srolovitz, and Y.-W. Zhang, Extrem. Mech. Lett. **9**, 215 (2016).
[46] Y. H. Xu and J. P. Wang, Adv. Mater. **20**, 994 (2008).
[47] R. E. Smallman and A. H. W. Ngan, *Modern Physical Metallurgy*, 8th ed. (Butterworth-Heinemann, 2013).
[48] W. D. Callister, Jr. and D. G. Rethwisch, *Fundamentals of Materials Science and Engineering—An Integrated Approach*, 5th ed. (Wiley, 2018).